

Analysis and simulation of a hybrid visible-light/infrared optical wireless network for IoT applications

THOMAS KAMALAKIS^{1,*}, ZABIH GHASSEMLOOY², STANISLAV ZVANOVEC³, AND LUIS NERO ALVES^{4,5}

¹Department of Informatics and Telematics, Harokopio University of Athens, Greece

²Northumbria Communication Research Lab (NCRLab), Northumbria University, Newcastle upon Tyne, UK

³Department of Electromagnetic Field, Czech Technical University in Prague, Czech Republic

⁴Department of Electronics Telecommunications and Informatics, University of Aveiro, Portugal.

⁵Instituto de Telecomunicações, Aveiro, Portugal.

*Corresponding author: thkam@hua.gr

Compiled November 8, 2021

We analyze the performance of a hybrid visible-light / infrared optical wireless communications network for indoor internet-of-things applications. This approach can be used to connect multiple battery-powered sensor nodes using low-cost infrared light emitting diodes to transmit data to a master node located at the ceiling of a room. The master node uses visible light communications to send back acknowledgments and coordinate the transmission. We present a detailed model for simulating the communications layer and energy usage, which is implemented in Python and is available under an open-source license. The results indicate the suitability of this approach for sporadically transmitting low data rate signals containing sensor readings in line with the massive machine-type communications fifth generation applications. © 2021 Optical Society of America

<http://dx.doi.org/10.1364/ao.XX.XXXXXX>

1. INTRODUCTION

The internet-of-things (IoT) [1] relies on interconnecting billions of devices and is currently being considered as one of the main drivers for the information and communication technology (ICT) industry. The fifth generation (5G) wireless networks regard massive machine-type communications (mMTC) as being one of the core application scenarios along with ultra reliable low latency communications (URLLC) and the extreme mobile broadband (eMBB) [2]. The mMTC networks deals with many low-power devices sporadically transmitting low data rate information in applications such as smart-grid [3], large-scale environments [4], structure monitoring [5], asset tracking [6], healthcare [7] and others.

Established IoT radio frequency (RF) communication technologies include WiFi, SigFox, cellular, IPv6 over the low-power wireless personal area networks (6LoWPAN), ZigBee, Bluetooth, RF identification (RFID) and Z-wave [8]. In addition, several alternative technologies at higher bands are being investigated including optical wireless communications (OWC) [9]. OWC rely on transmitting information in the visible and infrared (IR) wavelength ranges over the free space channel in both indoor and outdoor environments. The OWC technology combines the very large bandwidth of optical fibers and the flexibility of

RF wireless systems, inherent security at the physical layer, no interference with existing RF networks and limited adverse effects on the environment and living organisms. These aspects can be of high practical interest in special environments such as health-care [10] or industry [11].

OWC use cases in IoT are starting to attract attention including smart manufacturing [12], information proclaiming to the public [13], underwater IoT [14], intelligent transportation [15] and health-care [16]. Over the past years, we have seen the focus shifting from infrared (IR) systems to visible light communications (VLC), where light emitting diode (LED) lamps are used to provide both illumination and communication. In indoor applications, VLC is used for the down-link while the up-link is provided by some other technology [17]. Although WiFi is a likely candidate, one can reap the full benefits of OWC by using the IR for the uplinks. Up until now, IR systems have been considered cooperatively in the down-link [18] or the up-link for high-speed applications [19]. Considering the growing use of IoT devices in 5G and potentially in 6G wireless networks, and the potential use of the OWC technology, it essential to systematically evaluate its performance taking into account many application scenarios. IoT scenarios include a large number of interconnected nodes, e.g., sensor nodes (SNs) which will be battery-powered, thus making the energy efficiency a critical

factor in order to ensure longer battery replacement time. It is therefore important to analyze the implications of transceiver energy consumption. The main contribution of this work is the evaluation of the hybrid VLC/IR system for low-cost, low-speed indoor IoT communications in line with the 5G mMTC networks. We develop physical layer and energy usage models for SNs that send data to one or several master nodes (MNs) using low-cost IR LEDs in the up-link while MNs coordinate the SN transmissions at the down-link using VLC. Although similar physical layer communication models for such systems have been reported in the literature e.g., [2, 20], in this work in addition to various architectural characteristics such as transceiver positions, noise sources, etc, we include various application-specific parameters such as the nature and duration of the SN read-out, node battery life and the duration of the transmit cycle stages. The proposed complete end-to-end model is implemented in Python, and is freely available on the web under an open-source license [21]. For the first time, we consider two scenarios where the SN transmitters (TXs) are either narrow-beam or wide-beam and discuss their pros and cons within the context of IoT applications. We show that, the narrow-beam scenario is more suited for the case where the SNs are placed in fixed locations with SN/MN alignment being during installation, but at the cost of higher transmit power P_T and the increased energy usage. On the other hand using wider beams enables higher level of SN mobility. Using this model, we discuss the performance of the VLC/IR network in both scenarios. In summary, the work reported here advances the state-of-the-art in the field of OWC by: i) evaluating the communication performance and energy usage of low-cost VLC/IR for indoor IoT SN scenarios compatible with mMTC; ii) considering two distinct application scenarios related to the width of the optical beams; and iii) providing an open-source platform for further investigations of IoT-related OWC applications. To the best of authors' knowledge, no previous works have been reported in the literature covering these aspects.

The rest of the paper is organized as follows: in Section 2, we present the VLC/IR system in detail, while in Section 3 we outline the physical layer model. Section 4 discusses energy consumption and Section 5 provides indicative results for both the narrow and the wide-beam scenario considering the multiple access control (MAC) protocol performance as well. Some concluding remarks are given in Section 6.

2. THE HYBRID VLC/IR SYSTEM

The proposed hybrid system is most suited for interconnecting battery-powered SNs with MNs in an indoor environment, as illustrated in Fig. 1a. For the up-link, cost-effective IR LEDs are used between the SN and the MN, whereas for the down-link, LED-based VLC is utilized for coordinating SN transmissions and sending back the acknowledgment signals. The schematic diagram of the SN subsystems is depicted in Fig. 1b. At the receiver (RX), we use an optical rejection filter for limiting ambient light noise, a PIN photodiode and a transimpedance amplifier (TIA). At the TX, the sensor information is used for intensity modulating the IR LED(s) via the driver circuit. The node also contains the actual sensor(s) and the micro-controller unit (MCU). The MCU incorporates all the node intelligence including deciding when to put the node in a sleep mode in order to save power.

The MN architecture is similar except for the transmitting and receiving bands being interchanged. MN uses an LED for

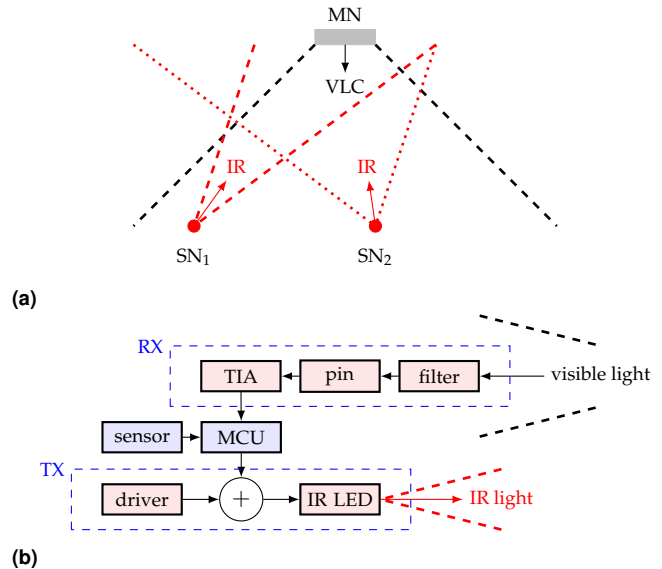


Fig. 1. (a) The hybrid VLC/IR network architecture and (b) the SN subsystem.

simultaneous communication and illumination with a sufficient coverage area to cater for all SNs. Note that in the case of larger rooms, multiple VLC LEDs can be used to ensure that all SNs are connected with at least one MN. Depending on the application considered, SNs could use narrow beam IR LEDs for the up-link, especially in cases where SNs are placed at fixed locations. In this case, the MN/SN alignment can be carried out once when the SN is installed. Alternatively, for SNs with mobility, one could use wider beam IR LEDs to provide higher tolerance in the MN/SN alignment at the cost of reduced received power P_R , i.e., worsened signal-to-noise (SNR) ratio. This requires the use of IR LEDs with higher P_T at the SNs to ensure sufficient SNR. Note that, angle diversity RXs could also be used to deal with SN mobility [22].

The MN is connected to the mains and hence there is no need to consider its power consumption in detail, whereas SNs are powered by batteries with a limited lifetime, which can be a crucial issue. As stated earlier, in the case of narrow beam IR LEDs, the required P_T will be lower thus leading to a reduced power consumption and an extended battery life. For wider beam IR LEDs, the battery life will be reduced due to the higher currents needed to obtain the same P_R at the MN. Here, we consider both scenarios in greater detail in the following sections.

3. THE PHYSICAL LAYER MODEL

In this section we describe the various aspects of the physical layer used in our study. We pay particular attention to the spectral characteristics of the SN transceiver shown in Fig. 1b, the LED power/current characteristic, the channel gain, the noise contributions at the RX and the estimation of the SNR. We also provide some indicative mathematical models for describing several aspects of the system, e.g., the optical power spectrum of the LEDs, etc. It is relatively straightforward to adapt different mathematical formulations or data measured experimentally.

A. LED TX

Fig. 2 shows the transmission spectra considered for the SN and the MN nodes. For the IR LED transmission spectrum of the SN,

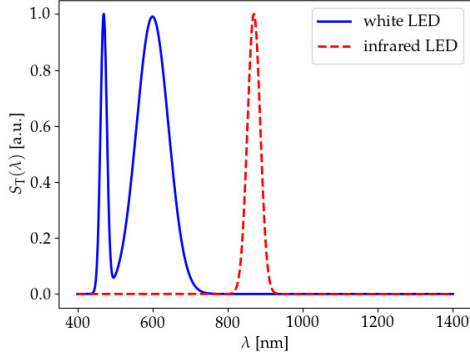


Fig. 2. Normalized transmission spectra for the LEDs considered.

we assume a Gaussian profile $S_T(\lambda) \propto \exp(-(\lambda - \lambda_I)^2/\sigma_I^2)$ with the central wavelength $\lambda_I = 870$ nm and $\sigma_I = \Delta\lambda_I/(2\sqrt{\ln 2})$, where $\Delta\lambda_I$ is the full width at half maximum (FWHM) and is assumed to be 40 nm. For the white phosphorescent LEDs, we must account for the blue and broader phosphor components [23]. We model the visible LED spectra as:

$$S_T(\lambda) \propto e^{-(\lambda - \lambda_B)^2/\sigma_B^2} + e^{-(\lambda - \lambda_P)^2/\sigma_P^2} \quad (1)$$

where λ_B and λ_P are the peak wavelengths for the blue and phosphor components at 470 and 600 nm respectively, while σ_B and σ_P are related to the FWHMs $\Delta\lambda_B$ and $\Delta\lambda_P$ of the blue and the phosphor component respectively, $\sigma_B = \Delta\lambda_B/(2\sqrt{\ln 2})$, $\sigma_P = \Delta\lambda_P/(2\sqrt{\ln 2})$. In this work we assume $\Delta\lambda_B = 20$ nm and $\Delta\lambda_P = 100$ nm. The spectrum matches a typical transmission spectrum of a warm white LED [23]. The total transmit power is given by:

$$P_T = \int_0^\infty S_T(\lambda) d\lambda \quad (2)$$

The radiation pattern of the LED determines the power budget between the nodes. The radiant optical intensity I_e , measured in W/sr, can be modeled using a generalized Lambertian pattern [24]:

$$I_e = P_T \frac{m+1}{2\pi} \cos^m \phi \quad (3)$$

where ϕ is the angle between the transmission direction and the direction of maximum transmission \mathbf{n}_S , m is the order of the pattern related to the angle of half intensity, $\Phi_{1/2}$ through:

$$m = -\frac{\ln 2}{\ln(\cos \Phi_{1/2})} \quad (4)$$

In this work, we assume $m = 1$ (i.e., $\Phi_{1/2} = 60^\circ$) for the VLC TX and two values for $\Phi_{1/2}$ for the IR LEDs: 10° for the narrow-beam SN ($m \approx 45$) and 60° ($m = 1$) for the wide-beam SN.

The LED power/current characteristic $P_T = g(I_D)$ determines the energy usage. At small current values, P_T increases linearly with I_D , but at higher current, the plot becomes non-linear. In this work we are more interested on the inverse power-current characteristic $I_D = f(P_T)$ and use a polynomial approximation:

$$I_D \approx \alpha_0 + \alpha_1 P_T + \alpha_2 P_T^2 + \dots \quad (5)$$

where α_i are obtained by least-square fitting. Fig. 3 shows the power-current plot of an IR LED and the approximation

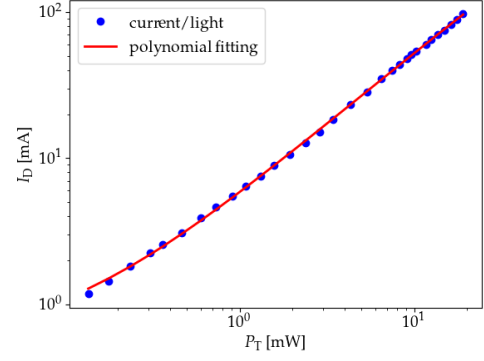


Fig. 3. Polynomial fitting of the inverse power-current characteristic of an IR LED.

obtained by fitting the values with a second-order polynomial. The coefficients obtained by least-square fitting the curve of a Vishay TSFF5210 IR LED are: $\alpha_0 = 5.61 \times 10^{-4}$ mA, $\alpha_1 = 5.32$ mA/mW and $\alpha_2 = -17.40$ mA/mW².

Note that, Eq. (5) applies for both VLC and IR LED assuming different polynomial coefficients α_i , but as we shall discuss next, the power-current characteristic is primarily important for the SNs, since it determines the current drawn from the node's battery. The up-link power budget determines the required optical power at the SNs. Eq. (5) can be used to estimate the required driving current for the IR LEDs.

B. Channel gain

Assuming a TX and a RX positioned at \mathbf{r}_S and \mathbf{r}_R respectively, with corresponding orientations along the unit vectors \mathbf{n}_S and \mathbf{n}_R , the channel gain is given as [25]:

$$h(\mathbf{r}_R, \mathbf{n}_R, \mathbf{r}_S, \mathbf{n}_S, m) = \frac{m+1}{2\pi R^2} \cos^m \phi \cos \theta A_{R \text{rect}} \left(\frac{\theta}{\text{FOV}} \right) \quad (6)$$

where

$$\cos \theta = \frac{\mathbf{n}_R \cdot (\mathbf{r}_S - \mathbf{r}_R)}{R} \quad (7a)$$

$$\cos \phi = \frac{\mathbf{n}_S \cdot (\mathbf{r}_R - \mathbf{r}_S)}{R} \quad (7b)$$

$$R = |\mathbf{r}_S - \mathbf{r}_R| \quad (7c)$$

and FOV and A_R is the field-of-view and area of the RX, respectively. Eq. (6) can be used for calculating the channel gain for both the up- and down-links. We have made the following assumptions: (i) a single MN with $m = 1$, located at the center of the ceiling $\mathbf{r}_{MN} = (L/2, W/2, H)$ and the SN is located at various positions on the floor $\mathbf{r}_{SN} = (x, y, 0)$ of a room with height $H = 3$ m and length and width $L = W = 5$ m; (ii) the MN is pointing downwards $\mathbf{n}_{MN} = (0, 0, -1)$ and SN is pointing towards the MN, $\mathbf{n}_{SN} = (\mathbf{r}_{MN} - \mathbf{r}_{SN})/|\mathbf{r}_{MN} - \mathbf{r}_{SN}|$; and (iii) $A_R = 1$ cm² and FOV = $\pi/2$ for both the SN and MN. The simulated channel gain distributions for the down-link (MS to SN) and up-link (SN to MS) are illustrated in Fig. 4 along the diagonal $\mathbf{r}'_{SN} = (x, x, 0)$ of the SN plane. Note that, the up-link gain is higher by ≈ 13 dB due to the larger m value of the SN TX.

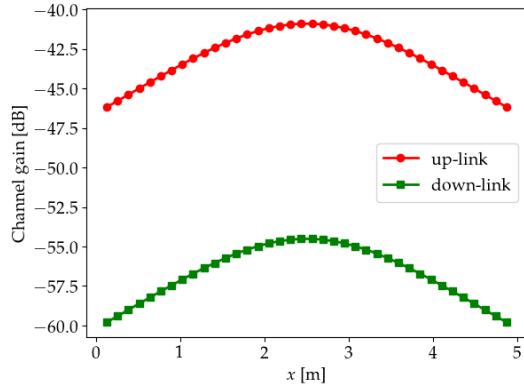


Fig. 4. Down-link and up-link channel gain along the diagonal of the SN plane

C. Optical RX

C.1. Wavelength response

At the RX side, we must account for the spectral response of the optical rejection filter $S_R(\lambda)$ required to limit ambient light interference. Fig. 5 shows a suitable optical rejection filter response, which is described by a super-Gaussian of order $p = 3$ as given by:

$$S_R(\lambda) \approx \exp\left(\left[-\frac{\lambda - \lambda_R}{\sigma_R}\right]^{2p}\right) \quad (8)$$

where λ_R is the center wavelength, and σ_R is related to the 10dB bandwidth B_R through $\sigma_R = B_R / (2 \sqrt[2p]{\ln 10})$. We assume λ_R , B_R at 870 and 300, and at 435 and 230nm for the VLC and IR rejection filters, respectively. These characteristics match reasonably well with the commercial RXs e.g., Excelitas VTB5051BH and Vishay BPV10NF. In addition, we also need to consider the wavelength

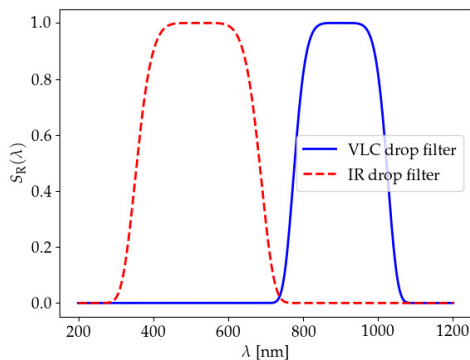


Fig. 5. Normalized optical filter characteristics considered at the RX side.

dependence of the detector responsivity $\mathcal{R}_p(\lambda)$. In this work, we have used polynomial fitting on values of \mathcal{R}_p of a commercial silicon PIN photodiode (e.g., Vishay BPV10NF) extrapolated from the datasheet, which is given as:

$$\mathcal{R}_p(\lambda) = \sum_{i=0}^{i=5} p_i \left(\frac{\lambda}{\lambda_{sc}}\right)^i \quad (9)$$

where the scaling wavelength $\lambda_{sc} = 710\text{nm}$ is taken as the middle of the wavelength range between 330 and 1090nm in which

\mathcal{R}_p is considered and the values of the coefficients p_i are given in Table 1. Fig. 6 shows the actual \mathcal{R}_p and its polynomial fitting. Note that, outside the wavelength range we have assumed $\mathcal{R}_p = 0$.

Table 1. Polynomial coefficients [A/W]

p_0	p_1	p_2	p_3	p_4	p_5
1.7	-12.8	36.0	-45.2	27.5	-6.4

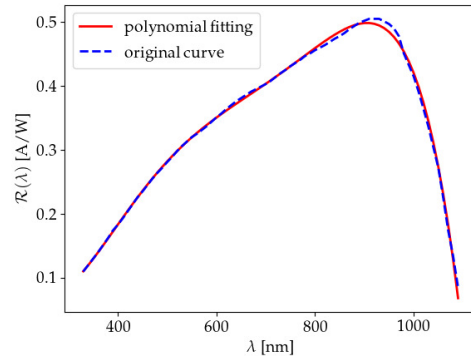


Fig. 6. Responsivity model assumed in this paper.

C.2. Spectral matching

The received power at the input and output of the optical filter is given by, respectively:

$$P_{in} = hP_T \quad (10a)$$

$$P_R = hc_{opt} \quad (10b)$$

where the coefficient c_{opt} is given by:

$$c_{opt} = \int_0^{\infty} S_R(\lambda) S_T(\lambda) d\lambda \quad (11)$$

The generated photocurrent is obtained through:

$$i_R = hc_{el} \quad (12)$$

where the coefficient c_{el} describes the matching of the transmission spectra $S_T(\lambda)$ to the overall wavelength response $\mathcal{R}_p(\lambda)S_R(\lambda)$ of the photo-detector and is given by:

$$c_{el} = \int_0^{\infty} \mathcal{R}_p(\lambda) S_R(\lambda) S_T(\lambda) d\lambda \quad (13)$$

Since S_T is normalized according to Eq. (2), c_{opt} and c_{el} are proportional to P_T . It therefore makes sense to define the normalized coefficients $\bar{c}_{opt} = c_{opt}/P_T$ and $\bar{c}_{el} = c_{el}/P_T$. In this context, \bar{c}_{opt} is the fraction of the incident optical power that reaches the optical filter output while \bar{c}_{el} is the effective responsivity accounting for the rejection filter of the RX and $\mathcal{R}_p(\lambda)$.

Based on Figs. 2, 5 and 6, we have obtained the values \bar{c}_{opt} and \bar{c}_{el} as given in Table 2. Also shown is the channel gain, assuming that the RX is positioned in the middle of the floor i.e., $\mathbf{r}_{SN} = (L/2, W/2, H)$. Using the normalized coefficients, we have:

$$P_R = h\bar{c}_{opt}P_T \quad (14a)$$

$$i_R = h\bar{c}_{el}P_T. \quad (14b)$$

Assuming P_T equal to 6W and 25mW for the MN and SN respectively, we have $P_R = 22.2\mu W$ and $P_R = 2.0\mu W$ at the MN and SN and $i_R = 6.7\mu A$ and $\approx 1\mu A$, respectively.

Table 2. Down-link and up-link parameters

Channel	TX	RX	h	\bar{c}_{opt}	\bar{c}_{el} [A/W]
down-link	MN	SN	3.53×10^{-6}	0.95	0.32
up-link	SN	MN	8.13×10^{-5}	0.99	0.49

C.3. Ambient light shot noise

The optical wireless system performance is mainly impaired by the natural and artificial ambient light sources including sunlight, lamps, etc. Depending on the actual environment conditions, the ambient light power at the RX can be many orders of magnitude larger than the received signal. Assuming a surface W such as a window allowing through the ambient light with spectral irradiance $s(\mathbf{r}, \lambda)$ measured in $W/m^2/nm$, then the power spectrum of the ambient light $s_{amb}(\lambda)$ measured in W/nm at the input of the RX filter is given as [25]:

$$s_{amb}(\lambda) = \int_W h(\mathbf{r}_R, \mathbf{n}_R, \mathbf{r}_S, \mathbf{n}_S, 1)s(\mathbf{r}_S, \lambda)d\mathbf{r}_S \quad (15)$$

The total ambient power at the filter output P_{amb} and the corre-

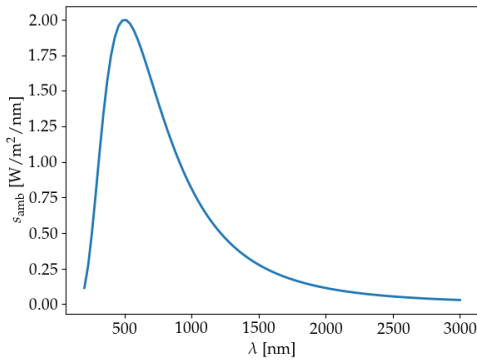


Fig. 7. Spectral irradiance model for sunlight

sponding photocurrent I_{amb} are determined by:

$$P_{amb} = \int_0^\infty s_{amb}(\lambda)S_R(\lambda)d\lambda \quad (16a)$$

$$I_{amb} = \int_0^\infty s_{amb}(\lambda)S_R(\lambda)\mathcal{R}_p(\lambda)d\lambda \quad (16b)$$

Fig. 7 shows the spectral irradiance s_{amb} of sunlight adopted in this paper. We assume a simple black-body radiation model [26] which is given by:

$$s(\lambda) = S_C \frac{2hf_0^3}{c^2} \frac{1}{e^{hf_0/k_B T_B} - 1} \quad (17)$$

where T_B is the absolute temperature of the black body, assumed to be 5800K [26] in our calculations, c is the speed of light, k_B is

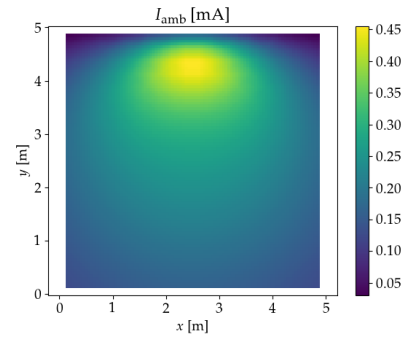


Fig. 8. Ambient light photocurrent I_{amb} .

Table 3. Ambient light spectral matching

RX	\bar{c}_{opt}	\bar{c}_{el} [A/W]
MN	0.19	0.09
SN	0.46	0.13

Boltzmann's constant, h_P is Planck's constant and f_0 is the optical frequency. The constant S_C is set so that the peak irradiance is equal to $2W/m^2/nm$.

In Table 3, we show the values of \bar{c}_{opt} and \bar{c}_{el} for the ambient light for the MN and SN RXs obtained as P_{amb}/P_{in} and I_{amb}/P_{in} , respectively, where P_{in} and P_{amb} are the ambient light powers at the input and the output of the optical filter while I_{amb} is the generated photocurrent. The MN is less susceptible to the ambient light noise since its RX operates in the IR range, where the sunlight spectral irradiance level is much lower. Fig. 8 shows the ambient light photocurrent I_{amb} assuming a window $1 \times 1m$ located at the south wall, centered at $r_w = (L/2, W, H/2)$ emitting ambient light with the spectral irradiance shown in Fig. 7. The RX is again considered at various positions in the floor with its direction aligned to the MN located at the middle of the ceiling. Artificial light sources may also contribute in the ambient light level. Under daylight conditions, we expect that this contribution will be much smaller than sunlight. For example in the case considered just after equation Eq. (14b), we obtained a photocurrent of the order of μA even at a high lamp power of 6W compared to the order of mAs shown in Fig. 8. The ambient light-induced shot-noise at the RX has a power spectral density (PSD) given as:

$$S_{shot}(f) = 2qeI_{amb} \quad (18)$$

where q_e is the electron charge. For the peak I_{amb} of 0.46mA in Fig. 8, we have $S_{shot} = 146pA^2/Hz$.

C.4. RX amplifier

We next consider the TIA of the RX. Fig. 9a shows a typical operational amplifier circuit [27] that can be used in the subsequent analysis. In the figure, C_D and R_D are the resistance and junction capacitance of the photodiode, respectively while R_F and C_F are the feedback resistance and capacitance. The internal voltage and current noise sources are v_n and i_n , respectively while the feedback resistance noise is v_{rn} and i_R is the generated photocurrent. Assuming no noise sources, an infinite open-loop gain for the amplifier and the negative port virtually grounded

the transimpedance is given as:

$$G_i = -\frac{v_{OUT}}{i_{IN}} \approx -Z_F = -\frac{R_F}{j2\pi f C_F R_F + 1} \quad (19)$$

where i_{IN} is the current at the input of the TIA and Z_F is the total impedance of the feedback circuit. The 3dB bandwidth of the amplifier is $B = (2\pi C_F R_F)^{-1}$. To analyze the noise at the output of the amplifier, we have assumed zero input ($i_R = 0$) and use Thevenin's theorem to simplify the feedback circuit as shown in Fig. 9b. In this figure $Z_D = R_D || (j2\pi f C_D)^{-1}$ and the equivalent impedance is $Z_{eq} = Z_F = R_F || (j2\pi f C_F)^{-1}$.

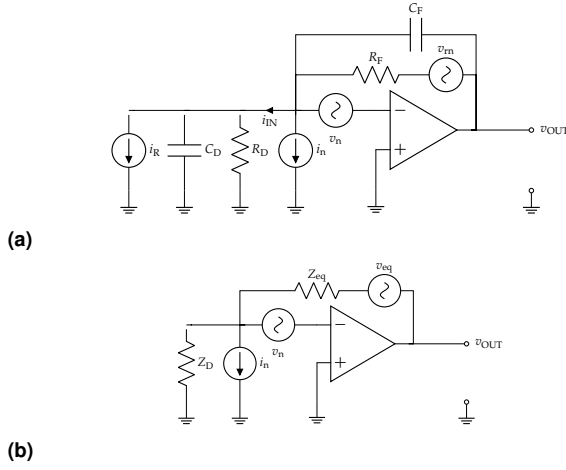


Fig. 9. RX TIA: a) full and b) equivalent circuits for noise analysis

The equivalent and the output voltage are given, respectively as:

$$v_{eq} = \frac{v_{rm}}{1 + j2\pi f C_F R_F} = \frac{Z_F}{R_F} v_{rm} \quad (20a)$$

$$v_{OUT} = v_{rm} \frac{Z_F}{R_F} - i_n Z_F - v_n \left(1 - \frac{Z_F}{Z_D}\right) \quad (20b)$$

The equivalent input current noise $n_I = -v_{OUT}/G_i$ is written as:

$$n_I = \frac{v_{rm}}{R_F} - i_n - v_n \left(\frac{1}{Z_F} - \frac{1}{Z_D}\right) \approx \frac{v_{rm}}{R_F} - i_n - \frac{v_n}{Z_F} \quad (21)$$

In the last equality we have assumed that $Z_D \gg Z_F$. The PSD of the amplifier noise in Eq. (21) is obtained as:

$$S_{amp}(f) = \frac{S_{RF}(f)}{R_F^2} + S_I(f) + \frac{S_V(f)}{|Z_F|^2} \quad (22)$$

where $S_V(f)$, $S_I(f)$ and $S_{RF}(f)$ are the PSDs of $v_{rm}(t)$, $i_n(t)$ and $v_n(t)$, respectively. $S_{RF}(f)$ is described by a standard white noise PSD which is given by:

$$S_{RF}(f) = 4k_B T_K R_F \quad (23)$$

$S_I(f)$ and $S_V(f)$ contain a white and a flicker noise component and are given by:

$$S_V(f) = V_{rms}^2 \left(1 + \frac{f_{cv}}{f}\right) \quad (24a)$$

$$S_I(f) = I_{rms}^2 \left(1 + \frac{f_{ci}}{f}\right) \quad (24b)$$

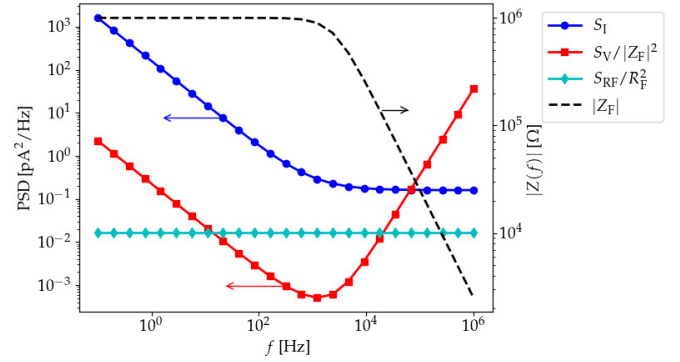


Fig. 10. PSD for various noise components

where V_{rms} and I_{rms} are the root mean square densities of the voltage and current noise with the corner frequencies of f_{cv} and f_{ci} , respectively.

Fig. 10 shows the PSD components in Eq. (22) assuming typical values $V_{rms} = 15nV/\sqrt{Hz}$, $I_{rms} = 400fA/\sqrt{Hz}$, $R_F = 1M\Omega$ and $C_F = 6.36nF$ resulting in $B = 2.5kHz$.

D. Signal-to-noise ratio

Assuming a simple on/off keying (OOK) modulation scheme, the signal to noise ratio can be calculated as:

$$SNR = \gamma^2 = \left(\frac{i_R}{2\sigma_n}\right)^2 \quad (25)$$

where σ_n^2 is the total noise power in terms of standard deviation accounting for both the shot and amplifier noise sources given by:

$$\sigma_n^2 = \int_B (S_{amp}(f) + S_{shot}(f)) df \quad (26)$$

where the bandwidth in terms of the data rate R_b is given as:

$$B = \frac{R_b}{e_{mod}} \quad (27)$$

and e_{mod} is the spectral efficiency of OOK which is assumed to be 0.4b/s/Hz. The bit error ratio (BER) is given by [25]:

$$P_e = Q(\gamma) \quad (28)$$

where Q is the Marcum-Q function [28] and γ is given by Eq. (25). This completes the specification of the physical layer model used in this work.

4. ENERGY USAGE

The estimation of the energy usage is important at SNs, since they use battery cells to power the sensor, MCU, TX and RX. To extend the battery life, we need to put each SN in a sleep mode when no data is being transmitted. Fig. 11 shows a typical cycle where, following a wake-up period t_{WU} , the MCU reads data from the node's sensor for a duration of t_{RO} and then transmits to the MN for a duration of t_{RX} . Next, the SN waits for the MN acknowledgment for a period of t_{TX} . The node then enters a sleep for a period of t_{SL} . The duration of each cycle is:

$$t_{CY} = t_{WU} + t_{RO} + t_{TX} + t_{RX} + t_{SL} \quad (29)$$

The actual values of the currents in Fig. 11 will depend on the implementation of transceiver circuit and MCU specifications.

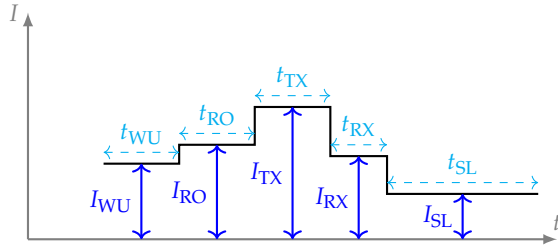


Fig. 11. SN cycle.

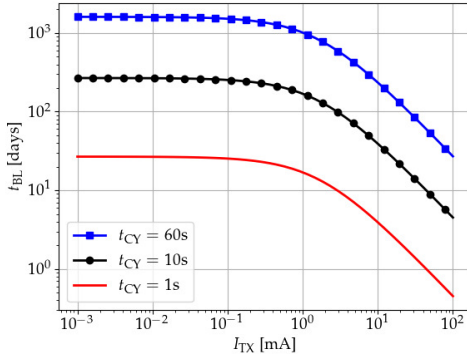


Fig. 12. Battery life dependence of a SN with respect to I_{TX} .

[29]. Commercial MCUs may consume as low as $I_{SL} \approx 400\text{nA}$ in the sleep mode. We assume the following: $t_{WU} \approx 20\text{ms}$, $t_{RO} \approx 40\text{ms}$ and $I_{WU} \approx I_{RO} \approx 1.3\text{mA}$. The current drawn during the transmission phase will be mainly due to the LED and reach as high as 100mA , depending on the LED type and the required P_T . We set $I_{TX} \approx \frac{1}{2}I_D + I_{WU}$ where I_D is the drive DC-current and the factor $\frac{1}{2}$ reflects equal number of binary one and zero, with zero power transmission for the zeros. The duration of the transmission phase for the up-link is $t_{TX} = L_{\text{data}}/R_b^u$, where L_{data} and R_b^u is the length and the data rate of the transmitted message, respectively. In the listening phase, we expect I_{RX} to be approximately equal to the quiescent current of the TIA, which can be as low as $1\mu\text{A}$, and the current drawn from the MCU. Hence $I_{RX} \approx I_{WU}$. The listening phase lasts $t_{RX} = L'_{\text{data}}/R_b^d$, where R_b^d is the data rate of the MN and L'_{data} the length of the acknowledgment message.

The charge Q_{CY} drawn from the battery in each cycle is given by:

$$Q_{CY} = i_{WU}t_{WU} + i_{RO}t_{RO} + i_{TX}t_{TX} + i_{RX}t_{RX} + i_{SL}t_{SL} \quad (30)$$

If Q_{TOT} is the supply battery capacity, then the battery life of each node is given by:

$$t_{BL} \approx \frac{Q_{TOT}}{Q_{CY}} t_{CY} \quad (31)$$

Fig. 12 depicts the dependence of the battery life with respect to the current I_{TX} in the transmission phase for two different cycle periods 1, 10, and 60s. We have assumed $R_b^u = R_b^d = 1\text{kb/s}$, $L_{\text{data}} = L'_{\text{data}} = 200\text{bits}$, and $Q_{TOT} = 220\text{mAh}$, which can be provided even by a coin-cell battery. From the figure, we clearly observe the strong effect of I_{TX} on the battery above 1mA . Battery life extension can be achieved using some additional energy

harvesting means in SNs. This can be relevant for SNs with mobility where energy harvesting methods such as triboelectric generators can be employed [30].

5. SYSTEM DESIGN AND PERFORMANCE

In this section, we estimate the performance of the hybrid optical wireless network based on the physical layer and energy usage models outlined in Section 3 and 4 respectively. We assume a threshold $\text{BER}_0 = 10^{-3}$, which is in the range of the forward error correction limit with $\gamma_0 = Q^{-1}(\text{BER}_0) \approx 3.1$ and $\text{SNR}_0 = \gamma_0^2 \approx 9.8\text{dB}$. The required transmit power is estimated from the power budget using Eq. (14b) in Eq. (25) and is given as:

$$P_{T0} = \frac{2\gamma_0\sigma_n}{h\bar{c}_{el}} \quad (32)$$

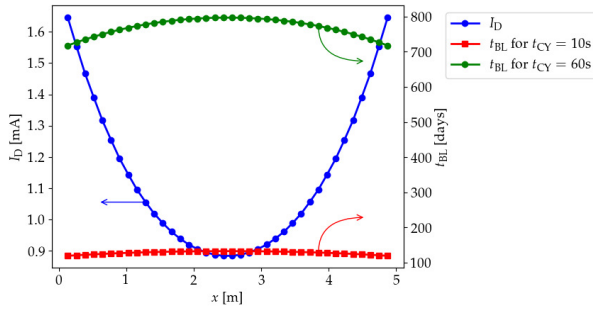
A. Narrow beam TX for the SNs

We first consider the narrow beam SN TXs, with $\Phi_{1/2} = 10^\circ$ and assuming their directions are aligned with the MN. For $R_b^u = R_b^d = 1\text{kb/s}$, we determine σ_n^2 using Eq. (26) taking into account Eq. (27), which yields $B = 2.5\text{kHz}$ for $e_{\text{mod}} = 0.4\text{b/s/Hz}$. We assume a single window as discussed in Section C.3 and use a simple trapezium rule to calculate Eq. (26). At the MN, we obtain $\sigma_n^2 = 6.41 \times 10^{-20}\text{A}^2$, where the dominant contribution is the shot noise ($= 6.05 \times 10^{-20}\text{A}^2$), which is higher than that of the amplifier noise (i.e., $3.63 \times 10^{-21}\text{A}^2$). In Fig. 13a, we show the required I_D calculated using Eq. (5), along the diagonal $\mathbf{r}'_{SN} = (x, x, 0)$. We also show the obtained t_{BL} for $t_{CY} = 10$ and 60s. We note that, the battery life is very long due to the small I_D of the order of 1mA , which are much smaller than currents drawn from commercial Zigbee and WiFi modules in transmission phase (tenths of mA) [31]. For $t_{CY} = 60\text{s}$ (transmission of one reading per minute), $t_{BL} > 700$ days for all SNs considered in the diagonal. The channel gain is higher near the center of the floor, leading to smaller P_T and consequently increased t_{BL} is increased for the central nodes. For a shorter $t_{CY} = 10\text{s}$ (one sensor reading every 10 seconds) t_{BL} is reduced but still remains >100 days for all nodes in the diagonal. Fig. 13b shows the distribution of the SN SNR for the VLC down-link for $P_T = 1\text{W}$. We observe higher SNR values for all positions considered on the RX plane. Since the VLC MN is connected to the mains and no battery is used, this implies that the down-link is excellent throughout the duration of t_{BL} .

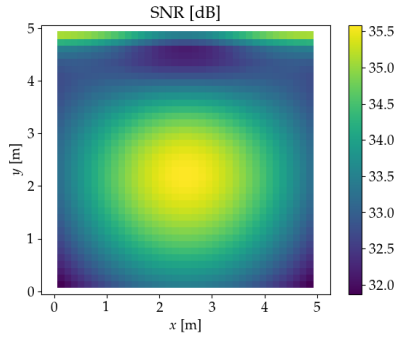
In view of potential mMTC applications, it is also interesting to calculate the maximum number N_{max} of devices that can be connected assuming that the channel utilization approaches unity, i.e. there are no idle periods between the SN transmissions. Since each node occupies the channel for an interval of $t_{\text{ac}} = t_{CY} - t_{SL}$ per cycle duration t_{CY} , the estimate for N_{max} is $N_{\text{max}} = t_{CY}/t_{\text{ac}}$. Using this estimate, we obtain $N_{\text{max}} \approx 130$ and ≈ 21 for $t_{CY} = 60\text{s}$ and 10s , respectively. Further increases in N_{max} can be obtained by increasing the specified data rate at the expense of higher P_T and hence lower battery life.

B. Wide beam sensor TXs

We now discuss a different scenario where wider beam TXs are used at the SNs. This has the effect of relaxing the need for aligning the SNs with the MN at the expense of higher transmit power. We assume that: (i) the order of the SN TX is $m = 1$ ($\Phi_{1/2} = 60^\circ$); and (ii) SNs are aligned vertically, i.e., $\mathbf{n}_{SN} = (0, 0, 1)$. Fig. 14a plots I_D and t_{BL} for SNs across the floor diagonal. Compared to the narrow-beam case, I_D is now higher, since P_T must be increased to compensate for the degraded link budget due to both

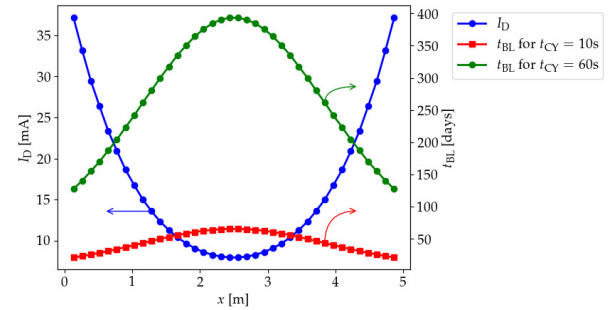


(a)

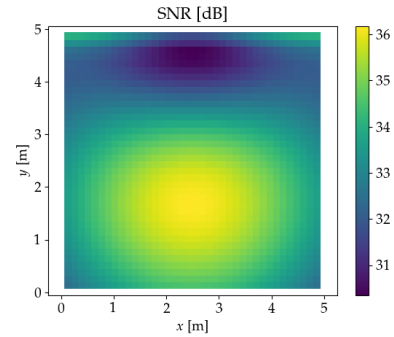


(b)

Fig. 13. (a) Required SN driving current and battery life, and (b) the achieved down-link SNR for the narrow beam sensor TXs.



(a)



(b)

Fig. 14. (a) Required SN driving current and battery life, and (b) the achieved down-link SNR in the wider beam scenario.

the misalignment between the SNs and the MN and the wider radiation pattern of the SNs. The values of I_D become comparable to the current values in of RF modules [31]. The battery life is reduced considerably but still remains high enough to be considered in practical applications especially when $t_{CY} = 60s$, where $t_{BL} > 100days$ for all SN positions. The down-link SNR is plotted in Fig. 14b. The misalignment between the SNs and the MN degrades the SNR compared to Fig. 13b, but remains higher than 30dB overall, thus implying excellent coverage at every position in the SN plane. We also note that, N_{max} is the same with that calculated in Section 5.A since the sensor cycles are identical.

C. MAC performance

We finally briefly discuss the impact of MAC performance on the SN battery life. In a typical MAC protocol such as the carrier-sense multiple access with collision avoidance (CSMA/CA) [32], we define the normalized (dimensionless) throughput S as the fraction of time the channel is being used to successfully transmit the payload bits. Using S , we obtain a more realistic estimate for $t_{TX} = L_{data} / (SR_b^u)$. As S decreases, t_{TX} increases thus implying a decrease in t_{BL} . Fig. 15 illustrates the impact of S on SN battery life for the narrow and wide-beam SNs, assuming $t_{CY} = 60s$. The curves labeled (C) and (E) correspond to SNs at the center and edge of the floor diagonal respectively. The influence of S is more severe in the wide-beam scenario since I_{TX} is higher and thus t_{BL} is more sensitive to the duration of the transmission period t_{TX} . For a typical value of $S = 0.8$ [32], we obtain a decrease of 18.7 and 15.7% for the central and edge wide-beam SNs that reduce to 11.9 and 10.9%, respectively for the narrow-beam SNs.

6. CONCLUSION AND OUTLOOK

The results of Section 5 indicate the suitability of the hybrid IR / VLC network for the low data rate IoT applications compatible with 5G mMTC. The narrow beam scenario implies an improved power budget due to the lower free space loss, provided the transceivers are carefully aligned. As mentioned in the introductory section, this is suitable for applications where the SNs are placed at fixed locations and alignment is ensured during installation. On the other hand, the wider beam scenario offers higher degree of SN mobility. Since we considered commodity (sub-euro) IR LEDs at low data rates and battery capacities that can be found in commercial coin cell batteries, we expect that the cost of implementing the actual SN components will be very low, thus rendering the solution economically viable. These arrangements can be used in a variety of application scenarios including hospital or remote patient monitoring, where OWC systems are embedded in wearables, high-precision location tracking in indoor environments such as malls and exhibits, asset tracking in warehouses, smart home automation and energy management systems and others. Depending on the mobility requirements of these applications the narrow-beam scenario can be considered, which significantly increases the battery life of the nodes. Although a full-blown comparison with other RF technologies is out of the scope of this paper, a first comparison indicates that the hybrid VLC/IR approach can lead to reduced power consumption (see discussion on Sections 5.A and 5.B), especially in the narrow beam scenario. Considering the other merits of OWC and namely zero interference with existing RF networks, the limited adverse biological effects and the inherent security, we believe that the VLC/IR system can be a viable candidate for mMTC IoT applications.

For the evaluations carried out in this paper, we developed

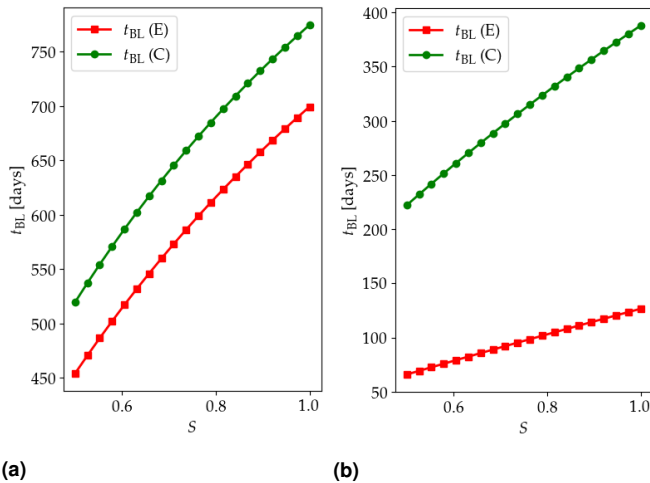


Fig. 15. Impact of S on t_{BL} for: (a) the narrow-beam and (b) narrow-beam scenarios. In the legends, (C) and (E) corresponds to SNs at the center or the edge of the floor diagonal, respectively

a full physical layer communication and power consumption model and the implementation is available on the web [21] under an open-source license. The model accounts for the various architectural parameters including node positioning, transceiver spectral characteristics, ambient and amplifier RX noise and the nature and duration of the SN read-out and transmit cycle stages. The model was implemented in Python, which will enable other researchers to evaluate this technology in various specific scenarios. There are several research questions that need addressing. For one, we need to ascertain that communication is possible even in the absence of non line-of-sight between the SN and the MN. This can be achieved due to the multipath nature of the optical wireless channel. We plan to address this in a future publication using a ray tracing simulation model for the impulse response of the channel. We may also consider scenarios where there are multiple lamps in the room that are used for MN and each SN communicates with the MN, which is closer by. We may also consider SNs with multiple IR LEDs pointing at different directions with a single transmitter being active, depending on the MN position and orientation. We briefly touched on the impact of the MAC protocol on the SN battery life. We plan to address MAC protocols based on time and frequency division multiple access (TDMA and FDMA) [33] as part of future research works. Finally, we need to consider the details of the hardware implementation and demonstrate this technology in practical use cases.

FUNDING

European Union COST Action Newfocus (CA19111)

REFERENCES

1. S. Nižetić, P. Šolić, D. L. d.-I. González-de, L. Patrono *et al.*, "Internet of things (iot): Opportunities, issues and challenges towards a smart and sustainable future," *J. Clean. Prod.* **274**, 122877 (2020).
2. J. Navarro-Ortiz, P. Romero-Diaz, S. Sendra, P. Ameigeiras, J. J. Ramos-Munoz, and J. M. Lopez-Soler, "A survey on 5g usage scenarios and traffic models," *IEEE Commun. Surv. & Tutorials* **22**, 905–929 (2020).

3. H. C. Leligou, T. Zahariadis, L. Sarakis, E. Tsampasis, A. Voukidis, and T. E. Velivassaki, "Smart grid: a demanding use case for 5g technologies," in *2018 IEEE International Conference on Pervasive Computing and Communications Workshops (PerCom Workshops)*, (IEEE, 2018), pp. 215–220.
4. R. Giuliano, F. Mazzenga, and A. Vizzarri, "Satellite-based capillary 5g-mmmtc networks for environmental applications," *IEEE Aerosp. Electron. Syst. Mag.* **34**, 40–48 (2019).
5. F. Franchi, F. Graziosi, A. Marotta, and C. Rinaldi, "Structural health monitoring over 5g urllc network," in *European Workshop on Structural Health Monitoring*, (Springer, 2020), pp. 60–68.
6. S. Horsmanheimo, J. Sää, T. Jokela, L. Tuomimäki, E. Nigusie, A. Hjelt, S. Huilla, T. Dönmez, N. Le Bail, and M. Valkama, "Remote monitoring of iot sensors and communication link quality in multisite mmmtc testbed," in *2019 IEEE 30th Annual International Symposium on Personal, Indoor and Mobile Radio Communications (PIMRC)*, (IEEE, 2019), pp. 1–7.
7. B. Wang, Y. Sun, C. Yuan, and X. Xu, "Lesla: A smart solution for sdn-enabled mmmtc e-health monitoring system," in *Proceedings of the 8th ACM MobiHoc 2018 Workshop on Pervasive Wireless Healthcare Workshop*, (2018), pp. 1–6.
8. S. Al-Sarawi, M. Anbar, K. Alieyan, and M. Alzubaidi, "Internet of things (iot) communication protocols," in *2017 8th International conference on information technology (ICIT)*, (IEEE, 2017), pp. 685–690.
9. H. Haas, J. Elmighani, and I. White, "Optical wireless communication," (2020).
10. D. R. Dhatchayeny, S. Arya, and Y. H. Chung, "Infrared-based multiple-patient monitoring in indoor optical wireless healthcare systems," *IEEE Sensors J.* **19**, 5594–5599 (2019).
11. N. Cong Hoan, N. Van Hoa, V. Thanh Luan, and Y. M. Jang, "Design and implementation of a monitoring system using optical camera communication for a smart factory," *Appl. Sci.* **9**, 5103 (2019).
12. M. Müller, D. Behnke, P.-B. Bök, C. Kottke, K. L. Bober, and V. Jungnickel, "Leverage lifi in smart manufacturing," in *2020 IEEE Globecom Workshops (GC Wkshps)*, (IEEE, 2020), pp. 1–6.
13. V. Jungnickel, M. Hinrichs, K. Bober, C. Kottke, A. Corici, M. Emmelmann, J. Rufo, P.-B. Bök, D. Behnke, M. Riege *et al.*, "Enhance lighting for the internet of things," in *2019 Global LIFI Congress (GLC)*, (IEEE, 2019), pp. 1–6.
14. G. Schirripa Spagnolo, L. Cozzella, and F. Leccese, "Underwater optical wireless communications: Overview," *Sensors* **20**, 2261 (2020).
15. X. Chen, J. Ding, B. Yu, H. Ma, and H. Lai, "A survey on wireless optical its for smart city," in *Asia Communications and Photonics Conference*, (Optical Society of America, 2019), pp. M4A–110.
16. S. Riurean, T. Antipova, Á. Rocha, M. Leba, and A. Ionica, "Vlc, occ, ir and lifi reliable optical wireless technologies to be embedded in medical facilities and medical devices," *J. medical systems* **43**, 1–10 (2019).
17. O. Bouchet, M. El Tabach, M. Wolf, D. C. O'Brien, G. E. Faulkner, J. W. Walewski, S. Randel, M. Franke, S. Nerreter, K.-D. Langer *et al.*, "Hybrid wireless optics (hwo): Building the next-generation home network," in *2008 6th International Symposium on Communication Systems, Networks and Digital Signal Processing*, (IEEE, 2008), pp. 283–287.
18. X. You, J. Chen, and C. Yu, "Efficient indoor data transmission with full dimming control in hybrid visible light/infrared communication systems," *IEEE Access* **6**, 77675–77684 (2018).
19. M. T. Alresheedi, A. T. Hussein, and J. M. Elmighani, "Uplink design in vlc systems with ir sources and beam steering," *IET Commun.* **11**, 311–317 (2017).
20. A. Al-Kinani, C.-X. Wang, L. Zhou, and W. Zhang, "Optical wireless communication channel measurements and models," *IEEE Commun. Surv. & Tutorials* **20**, 1939–1962 (2018).
21. T. Kamalakis, "Pyowiot," <https://github.com/thomaskamalakis/pyowiot> (2021).
22. M. T. Alresheedi and J. M. Elmighani, "Hologram selection in realistic indoor optical wireless systems with angle diversity receivers," *J. Opt. Commun. Netw.* **7**, 797–813 (2015).
23. S.-W. Wang, F. Chen, L. Liang, S. He, Y. Wang, X. Chen, and W. Lu, "A high-performance blue filter for a white-led-based visible light communication system," *IEEE wireless communications* **22**, 61–67 (2015).

24. J. R. Barry, J. M. Kahn, W. J. Krause, E. A. Lee, and D. G. Messerschmitt, "Simulation of multipath impulse response for indoor wireless optical channels," *IEEE journal on selected areas communications* **11**, 367–379 (1993).
25. J. M. Kahn and J. R. Barry, "Wireless infrared communications," *Proc. IEEE* **85**, 265–298 (1997).
26. R. M. Goody and Y. L. Yung, *Atmospheric radiation: theoretical basis* (Oxford university press, 1995).
27. A. Kay, *Operational amplifier noise: techniques and tips for analyzing and reducing noise* (Elsevier, 2012).
28. G. P. Agrawal, *Fiber-optic communication systems*, vol. 222 (John Wiley & Sons, 2012).
29. J. Borgeson, S. Schauer, and H. Diewald, "Benchmarking mcu power consumption for ultra-low-power applications," *Tex. Instruments* (2012).
30. C. Wu, A. C. Wang, W. Ding, H. Guo, and Z. L. Wang, "Triboelectric nanogenerator: a foundation of the energy for the new era," *Adv. Energy Mater.* **9**, 1802906 (2019).
31. O. O. Kazeem, O. O. Akintade, and L. O. Kehinde, "Comparative study of communication interfaces for sensors and actuators in the cloud of internet of things," *Int. J. Internet Things* **6**, 9–13 (2017).
32. E. Ziouva and T. Antonakopoulos, "Cdma/ca performance under high traffic conditions: throughput and delay analysis," *Comput. communications* **25**, 313–321 (2002).
33. P. Huang, L. Xiao, S. Soltani, M. W. Mutka, and N. Xi, "The evolution of mac protocols in wireless sensor networks: A survey," *IEEE communications surveys & tutorials* **15**, 101–120 (2012).

AUTHOR BIOGRAPHIES

Thomas Kamalakis received his BSc, MSc and PhD from the National and Kapodistrian University of Athens. He is currently a professor at the Department of Informatics and Telematics of Haropokio University of Athens where he also serves as the Head of the Department. He has over 100 publications in the field of optical wireless, nanophotonic and network technoeconomics.

Zabih Ghassemlooy (Fellow, SOA; Fellow, IET; Senior Member, IEEE; Member, ACM), CEng, BSc(Hons.), MMU, (1981), MSc (1984) and PhD (1987) Manchester Univ., UK. 1987-88 Post-Doctoral Research Fellow, City Univ., UK. 1988-2004 Sheffield Hallam University and 2004-14 Northumbria University (NU), UK, and is Head of Optical Communications Research Group. He is Research Fellow (2016-) and Distinguished Professor (2015-) at Chinese Academy of Science, Vice-Chair of Cost Action-CA19111, 2020-24. 940 publications. Research interest: optical wireless communications (OWC) and hybrid RF-OWC. Chief Editor: *British J. of Applied Science and Technology* and *Intern. J. of Optics and Applications*. Vice-Chair of OSA Technical Group (Optics in Digital Systems-2018-).

Stanislav Zvanovec received the M.Sc. and Ph.D. degrees from the Faculty of Electrical Engineering, Czech Technical University (CTU) in Prague, in 2002 and 2006, respectively. He is currently works as a Full Professor, the Deputy Head of the Department of Electromagnetic Field. His current research interests include free space optical (FSO) systems, visible light communications (VLC), fiber optical systems systems and sensors, RF (millimeter wave) over optics (RoF and RoFSO). He is the author of two books (and coauthor of the book *Visible Light Communications: Theory and Applications*), several book chapters and more than 300 journal articles and conference papers.

Luis Nero Alves is IEEE member since 2003. Graduated in 1996 and received his MSc degree in 2000, both in Electronics and Telecommunication Engineering from the University of Aveiro.

Obtained the PhD degree in Electrical Engineering from the University of Aveiro in 2008. His expertise is on integrated circuit design for optical wireless applications. Since 2008 he has been the lead researcher from the Integrated Circuits group at Instituto de Telecomunicações, Aveiro. His current research interest are associated to the design and performance analysis of optical wireless communication systems, with special flavor in visible light communications. Other research topics include materials and devices for IoT sensing devices. He has authored and coauthored several research articles in these fields. Luis Nero Alves has participated/coordinated several research projects in the fields of optical wireless communications and sensing devices (with both national funding – FCT/VIDAS, FCT/EECCO, IT/VLCLighting - and international funding – EU-CIP/LITES, EU-FP7/RTMGear, EU-COST/OPTICWISE, EU-COST/MEMOCIS, EU-/H2020/MSCA/VisIoN, EU-H2020/FET/NeuralStimSpinal). Luis Nero Alves has also served in the technical program committee of several international conferences on the field of optical wireless communications. He has also served as reviewer for several journals in Optical communications, amongst which, *IEEE/PTL*, *IEEE-OSA/JLT* and *Elsevier/OC*.